

RESEARCH

Open Access



Flexible multilevel nonvolatile biocompatible memristor with high durability

Xiaoping Chen¹, Xu Zhao¹, Xiaozhong Huang¹, Xiu-Zhi Tang⁴, Ziqi Sun^{2*}, Da-Long Ni^{3*}, Hailong Hu^{5*} and Jianling Yue^{1*}

Abstract

Current protein or glucose based biomemristors have low resistance-switching performance and require complex structural designs, significantly hindering the development of implantable memristor devices. It is imperative to discover novel candidate materials for biomemristor with high durability and excellent biosafety for implantable health monitoring. Herein, we initially demonstrate the resistance switching characteristics of a nonvolatile memristor in a configuration of Pt/AIOOH/ITO consisting of biocompatible AIOOH nanosheets sandwiched between a Indium Tin Oxides (ITO) electrode and a platinum (Pt) counter-electrode. The hydrothermally synthesized AIOOH nanosheets have excellent biocompatibility as confirmed through the Cell Counting Kit-8 (CCK-8) tests. Four discrete resistance levels are achieved in this assembled device in responsible to different compliance currents (I_{CC}) for the set process, where the emerging multilevel states show high durability over 10^3 cycles, outperforming the protein-based biomemristors under similar conditions. The excellent performance of the Pt/AIOOH/ITO memristor is attributed to the significant role of hydrogen proton with pipe effect, as confirmed by both experimental results and density functional theory (DFT) analyses. The present results indicate the nonvolatile memristors with great potential as the next generation implantable multilevel resistive memories for long-term human health monitoring.

Keywords Implantable memristors, AIOOH nanosheets, Information storage, Multilevel

*Correspondence:

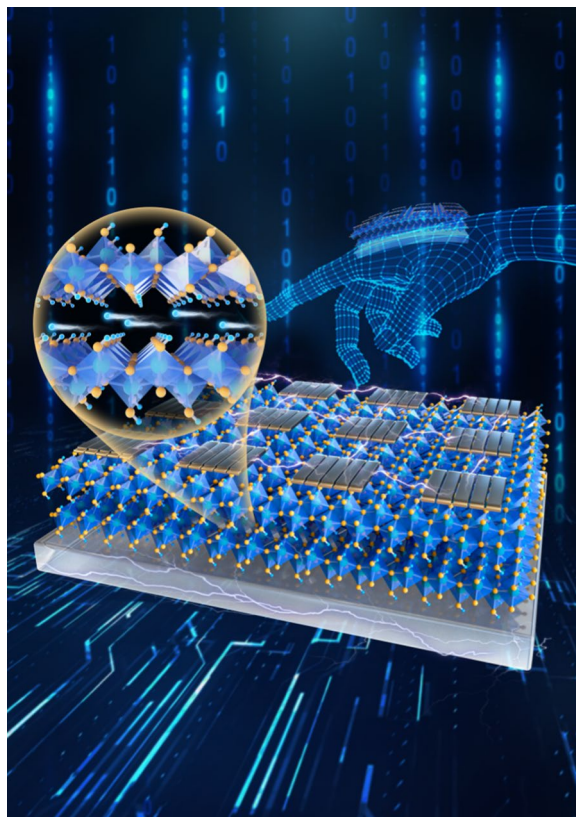
Ziqi Sun
ziqi.sun@qut.edu.au
Da-Long Ni
ndl12353@rjh.com.cn
Hailong Hu
hailonghu@csu.edu.cn
Jianling Yue
jlyue2010@csu.edu.cn

Full list of author information is available at the end of the article



© The Author(s) 2023. **Open Access** This article is licensed under a Creative Commons Attribution 4.0 International License, which permits use, sharing, adaptation, distribution and reproduction in any medium or format, as long as you give appropriate credit to the original author(s) and the source, provide a link to the Creative Commons licence, and indicate if changes were made. The images or other third party material in this article are included in the article's Creative Commons licence, unless indicated otherwise in a credit line to the material. If material is not included in the article's Creative Commons licence and your intended use is not permitted by statutory regulation or exceeds the permitted use, you will need to obtain permission directly from the copyright holder. To view a copy of this licence, visit <http://creativecommons.org/licenses/by/4.0/>. The Creative Commons Public Domain Dedication waiver (<http://creativecommons.org/publicdomain/zero/1.0/>) applies to the data made available in this article, unless otherwise stated in a credit line to the data.

Graphical Abstract



Introduction

Memristors are one of the most promising candidates for the next-generation of non-volatile memories in logic operations and brain neural function modeling [1–3]. The increasing demand for the real-time and long-term monitoring of human health in recent years has stimulated great interest in implantable memristors with feature resistance-switching characteristics and biocompatibility [4, 5]. Presently, a wide range of materials have been demonstrated to show resistance switching properties, including inorganic metal-oxides, metal chalcogenides, and organic natural biomaterials. Specifically, natural biomaterials as proteins or glucose as representatives have been regarded as the leading candidates to build the next generation of implant memristors, owing to their excellent biocompatibility [6]. Most current protein or glucose based biomemristors (Additional file 1: Fig. S1), [7–17] however, exhibit poor resistance switching performances, such as low endurance (<500 cycles), high variability, and usually need to match active electrodes (Ag, Al, W, Cu), which have substantially hindered the development of implantable memristor devices. Meanwhile, the solubility

characteristic of proteins or glucose renders this class of biomemristors, which are unsuitable for long-term information storage in the living body. In addition, the existing biomemristors generally demonstrate only single-level or mostly not exceed three-level resistive switching characteristics, which limit the data storage density. It is acknowledged that the multi-level cell characteristics of memristors responded towards the I_{CC} during set operation can offer a unique opportunity to achieve more than 2-bits of storage in a single device [18, 19], and thus significantly enhancing the data storage density [20]. Therefore, to meet the rigorous demands of future implantable memristors, it is imperative to develop novel biomemristors with highly sensitive and durable resistive switching performance and good biocompatibility.

In this work, a flexible, highly sensitive and durable biomemristor based on a layered structure material, ALOOH nanosheets, is innovated to realize multi-resistive memristive characteristics and good biocompatibility. Compared with other biomemristors, ALOOH-based memristors present highly responsible multilevel resistance states and environmental stability, and exhibit a

great potential for next generation long-term storage and information classification of human body for implantable health monitoring. The key component, Boehmite or aluminium oxide hydroxide (γ -AlOOH), possesses a large number of out-of-plane hydrogen atoms to form hydrogen bonding networks and maintain the integrity of the layered structure [21, 22] and allows rapid proton transport through the hydrogen-bond proton-transfer channels [23]. Owing to its particular structure, γ -AlOOH has shown versatile potential applications in the fields of biomedicine, environmental remediations, electrochemical energy conversions, optical nanodevices, etc. It is noted that γ -AlOOH has an excellent biosafety record, which is a common inorganic adjuvant among various human vaccines approved by the American Food and Drug Administration (FDA) [24, 25]. Meanwhile, γ -AlOOH is also an advanced antibacterial material [26]. All these features indicate that γ -AlOOH could be a very promising candidate material for implantable devices. However, there few reports on the application of γ -AlOOH into the implantable memristors to date, and the mechanisms in regards to proton transfer and the contributions of the proton conduction with hydrogen to the resistance switching effect remain unclear. Recently, Yao et al. demonstrated a resistive random-access memory (RRAM) device based on a metal–organic framework (MOF) material, FJU-23-H₂O [23]. Ascribed to a voltage-gated proton conduction with hydrogen bond pathways instead of oxygen-ion migration, resistive switching properties have been verified, which may bring some clues for the understanding of γ -AlOOH-based memristors. Therefore, contributed by the migration of hydrogen protons in shaping the resistance switching behaviors, a flexible multilevel nonvolatile biocompatible γ -AlOOH-based memristor is designed for highly sensitive, bio-safe, and environmentally durable implantable health monitoring. It is expected that this study will inevitably offer new insights into the development of next generation flexible implantable biomemristors for durable and biosafe healthy monitoring.

Results and discussion

Schematic of memristive device structure and cross-sectional SEM image of the Pt/AlOOH/ITO device are presented in Fig. 1a. The memristor comprises fluorine-doped tin oxide (ITO) as one electrode and platinum (Pt) (≈ 85 nm) as the other electrode with AlOOH film (≈ 300 nm) sandwiched in between. The response characteristics of the Pt/AlOOH/ITO memristor were recorded under different compliance currents and applied bias voltages. As shown in Fig. 1b, four different I-V curves of the configured device of Pt/AlOOH/ITO can be distinctly achieved to reach the compliance currents (I_{CC}) of 1 mA, 2 mA, 4 mA, and 6 mA, respectively under the

DC voltage sweep of $0\text{ V} \rightarrow 3\text{ V} \rightarrow 0\text{ V} \rightarrow -3\text{ V} \rightarrow 0\text{ V}$. The four different I-V curves in Fig. 1b show that a lower reset current can be obtained by using a lower I_{CC} . This proves that the use of different I_{CC} in the set process for the AlOOH based memristor contributes to multilevel low resistance states, showing its applicability to multi-bit storage in one device. At the same time, the device has extremely high sensitivity to I_{CC} changes. And the resistance value of the device changes significantly only by changing a small I_{CC} change. In addition, the device exhibits the same multilevel low resistance states (Additional file 1: Fig. S2a–c) under the DC voltage sweep of $0\text{ V} \rightarrow 4\text{ V} \rightarrow 0\text{ V} \rightarrow -4\text{ V} \rightarrow 0\text{ V}$. This confirms the feasibility that the storage density of the device can be further improved.

The switching between low and high resistance states is found to be highly stable. Figure 1c shows the switching voltage distributions in its four states over a total of 120 cycles. It is found that V_{set} is concentrated at $2.27 \pm 0.29\text{ V}$ and V_{reset} is concentrated between $-1.20 \pm 0.16\text{ V}$ under the DC voltage sweep of $0\text{ V} \rightarrow 3\text{ V} \rightarrow 0\text{ V} \rightarrow -3\text{ V} \rightarrow 0\text{ V}$. Therefore, it can be concluded that the switching voltage of the device in the four states is relatively confined within a narrow value range, demonstrating the desired stability of the device.

To further evaluate the reliability of the four states of the device, its endurance and retention tests were carried out under four different currents ($I_{CC} = 1\text{ mA}, 2\text{ mA}, 4\text{ mA}$ and 6 mA), as shown in Fig. 1d. Note that the test read voltage is 0.5 V and the loading voltage are 3 V and -3 V respectively. Figure 1d shows that the resistance of high resistance state (HRS) shows no pronounced variation with different I_{CC} , whereas the resistance of low resistance state (LRS) significantly decreases with the increasing I_{CC} , which further confirms the device has a high sensitivity for the change of I_{CC} . As a result, the endurance of the device under each individual I_{CC} of $1\text{ mA}, 2\text{ mA}, 4\text{ mA}$ and 6 mA has surpassed 1000 cycles, with no degradation being observed, showing the strong robustness and reliability of the four resistance states in this operating device. Figure 1e shows the retention characteristic of the corresponding resistance state of the device under four different orders of I_{CC} ($1\text{ mA}, 2\text{ mA}, 4\text{ mA}$ and 6 mA), where the resistance was read every 1 s with a voltage of 0.5 V . It is found that the retention time of the four resistance states all exceeded 3200 s , indicating its multiple stable intermediate resistance states. Therefore, RRAM device with AlOOH shows great potential in multi-density storage as evidenced by both retention and endurance performance test.

To evaluate the effectiveness of the device in multi-resistance state storage, the cyclability of the device under different I_{CC} was also studied. The results show that the

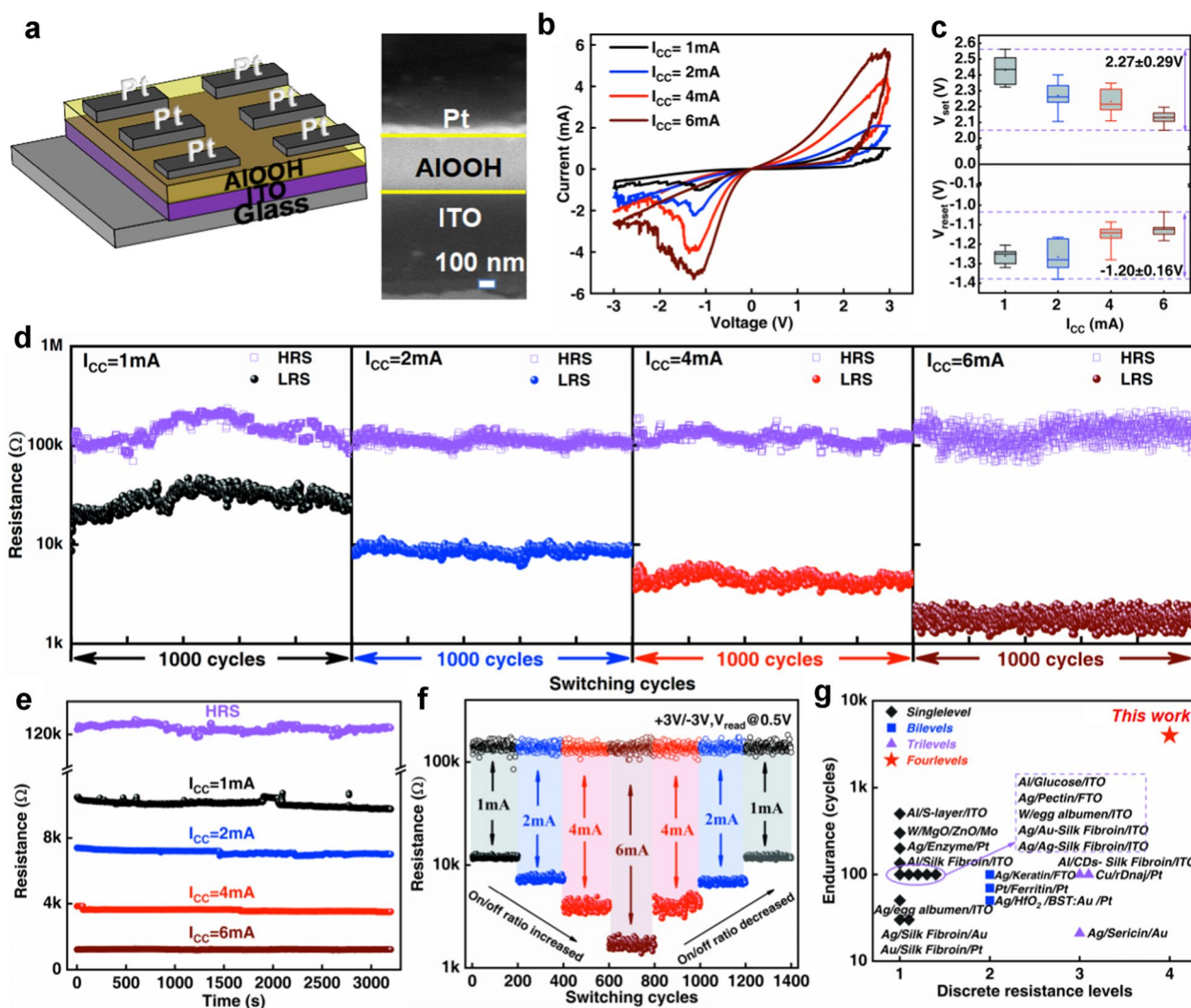


Fig. 1 Memristive behavior of Pt/AIOOH/ITO device. **a** Two-terminal memristive device in Pt/AIOOH/ITO configuration (left) and cross-sectional SEM image of the Pt/AIOOH/ITO device (right). **b** Four different I-V curves of the device at different levels of I_{CC} (1 mA, 2 mA, 4 mA and 6 mA), and each I-V curves has a different LRS/HRS ratio. **c** Switch voltage distributing in its 4 states, a total of 120 cycles. **d** Repeatability test of the HRS and LRS values of the fabricated device under four different orders of magnitude of I_{CC} (1 mA, 2 mA, 4 mA and 6 mA). The endurance of the device over 10^3 cycles at “On” and “Off” states respectively in all four states. **e** The retention time of the four resistance states all exceeded 3.2×10^3 s. A read voltage of 0.5 V was used for the measurement. **f** The resistance of the device over 1400 cycles under the I_{CC} sweep of 1 mA \rightarrow 2 mA \rightarrow 4 mA \rightarrow 6 mA \rightarrow 4 mA \rightarrow 2 mA \rightarrow 1 mA. **g** The comparison of the endurance and discrete resistance levels between AIOOH and other representative RRAM implantable materials, as presented in Additional file 1: Table S1

device achieves four discrete resistance levels that can be apparently distinguished by using different I_{CC} for the set process and further investigation shows that four resistance levels of AIOOH based memristor can be switched stably under each individually applied I_{CC} of 1 mA, 2 mA, 4 mA and 6 mA, as shown in Fig. 1f. Surprisingly, the device can stably circulate 1400 cycles under the I_{CC} sweep of 1 mA \rightarrow 2 mA \rightarrow 4 mA \rightarrow 6 mA \rightarrow 4 mA \rightarrow 2 mA \rightarrow 1 mA, which is distinctly higher than the values (about 21–22 cycles) previously reported on protein and related

similar types of biomemristors [8, 14]. This verifies that four storage states of the device are completely reversible. To this end, the potential of AIOOH based resistance switching memory device for multi-level memory has been demonstrated.

To show the potential applications of our fabricated AIOOH based device, the devices based on AIOOH and some representative implantable or bio-compatible materials including the inorganic and organic media are compared in Fig. 1g and Additional file 1: Table S1 [7–17,

27–34]. First, ALOOH demonstrates the highest endurance value in implantable memristors, which also shows its superiority compared to that of other reported organic and in-organic based devices. Secondly, the ALOOH based device can successfully function and survive up to four levels of I_{CC} followed by multiple stable intermediate resistance states, which can be repeated with high endurance ($>10^3$ cycles). Other implantable or bio-compatible materials can only survive up to max three levels of I_{CC} and do not show multi-resistance states that can be switched stably. The set voltage of ALOOH device is about 2.27 V without the conventionally applied electroforming voltage, which is lower than most biological materials. Among the comparable candidates, Pt/ALOOH/ITO device thus demonstrates excellent endurance performance with the highest cycling values (four states all $>10^3$), as well as multilevel memory operation and good retention performance under the small I_{CC} range. In addition, the device shows a competitive transparency of over 88% under visible light. Therefore, ALOOH-based memristors show great utility in wearable or implantable applications owing to their stable memristive performance.

Figure 2a shows the morphology of ALOOH nanosheets under low-magnification TEM, whose monolithic morphology is close to a square shape (Additional file 1: Fig. S3a). Additional file 1: Fig. S3b shows the particle size of ALOOH nanosheets falling in the range of 75–85 nm in statistics based on analysis of Fig. 2a. Figure 2b shows the corresponding element mapping of Al and O in ALOOH nanosheets whose element ratio is approximately 1:2. Additional file 1: Fig. S3c is the image of HAADF-STEM, where ALOOH nanosheets are stacked with a layered structure. Specifically, from Additional file 1: Fig. S3d–f and Fig. 2c, the surface of ALOOH film prepared through the drip coating method is relatively flat, where ALOOH nanosheets in the film layer do not indicate the obvious agglomeration, showing a stacking uniformly. Figure 2d depicts the high-resolution TEM image of the ALOOH crystal lattice of ALOOH. The ALOOH crystal surface spacing is 0.63 nm, which is corresponding to the (0 2 0) plane of ALOOH. The corresponding fast Fourier transform (FFT) pattern indicates that the basal plane of the ALOOH is the (0 2 0) plane (inset of Fig. 2d). These are consistent with the X-ray diffraction (XRD) pattern result presented in Fig. 2e. The XRD result suggests that observed diffraction peaks are all consistent with standard JCPDF No. 83-2384, indicating the pure ALOOH phase. The obtained ALOOH belongs to the orthorhombic cell with lattice parameters of $a=3.69$ Å, $b=12.21$ Å, and $c=2.87$ Å [35]. Narrow reflection peaks of (020), (120) and (031) are demonstrated, which are corresponding to the formation of the γ -ALOOH phase with a high

crystallinity. Therefore, high purity of ALOOH is achieved with uniform structure.

The chemical state of atoms in the prepared sample is studied by X-ray photoelectron spectroscopy (XPS). The XPS spectra of Al 2p, Al 2s, C 1s and O 1s regions in ALOOH is shown in Fig. 2f. Carbon decomposition occurs during the charging correction, as can be revealed by the C 1s XPS spectrum. Two peaks at 74.5 and 119 eV are Al 2p and Al 2s in ALOOH [36]. The peaks at 531.7 and 532.8 eV are attributed to the lattice oxygen (O 1s) of ALOOH and the oxygen of surface hydroxyl (OH) groups, respectively [37]. The O 1s spectra is deconvoluted into three peaks, which are corresponding to the three types of oxygen species. In Fig. 2g, the peaks at 530.6–530.7, 532.0–532.1, and 533.1–533.2 eV are attributed to bulk oxygen from the crystal structure (Al–O, 28.4%), surface hydroxyl groups (Al–OH, 53.1%), and adsorbed water on the surface (H–OH, 18.5%) [38]. High amount of hydroxyl groups on ALOOH is reflected by the $O_{OH}/O_{Lattice}$ ratio of 65%. In conjunction with the crystal structure of ALOOH, ALOOH is confirmed with a large number of hydrogen bonds. At the same time, ALOOH contains almost no oxygen vacancies from the O 1s spectra deconvoluted, which is different from traditional oxide materials.

To verify the rationality of the peak splitting of O 1s, Fourier transform infrared (FTIR) is used to further characterize the prepared ALOOH nanosheets, as shown in Fig. 2h. The bands at approximately 1082 cm^{-1} and 1152 cm^{-1} represent the (OH)–Al=O asymmetric stretching and the O–H bending, respectively, which are the typical characteristic of ALOOH. The absorption peaks at 563 cm^{-1} , 641 cm^{-1} and 753 cm^{-1} are attributed to the stretching vibration mode of AlO_6 [39]. The weak band at 1640 cm^{-1} is attributed to the stretching and bending modes of adsorbed water molecules despite the very weak absorbance in the ALOOH nanostructure spectrum, indicating that the number of physically adsorbed water molecules is quite few [40]. The asymmetric and symmetric stretching of the interlayer OH groups are observed at 3282 and 3090 cm^{-1} , respectively [41]. This is consistent with the result of the O 1s spectra deconvoluted of XPS. Interestingly, the transmittance curve of the ALOOH film demonstrates a transparency of over 88% under visible light at a wavelength range of 350–800 nm (in Fig. 2i). ALOOH film is competitive in transmittance when compared to that of other transparent materials, such as ZnO, TaO_x, protein, etc. [15, 17, 42, 43].

Figure 3a shows the cyclic current–voltage (I–V) characteristics of the device, which was obtained at the 4 mA by the DC voltage sweep of 0 V \rightarrow 3 V \rightarrow 0 V \rightarrow -3 V \rightarrow 0 V. The device was initially in the OFF state, exhibiting high resistance. When the applied voltage exceeded the set voltage ($V_{set} \sim 2$ V), the

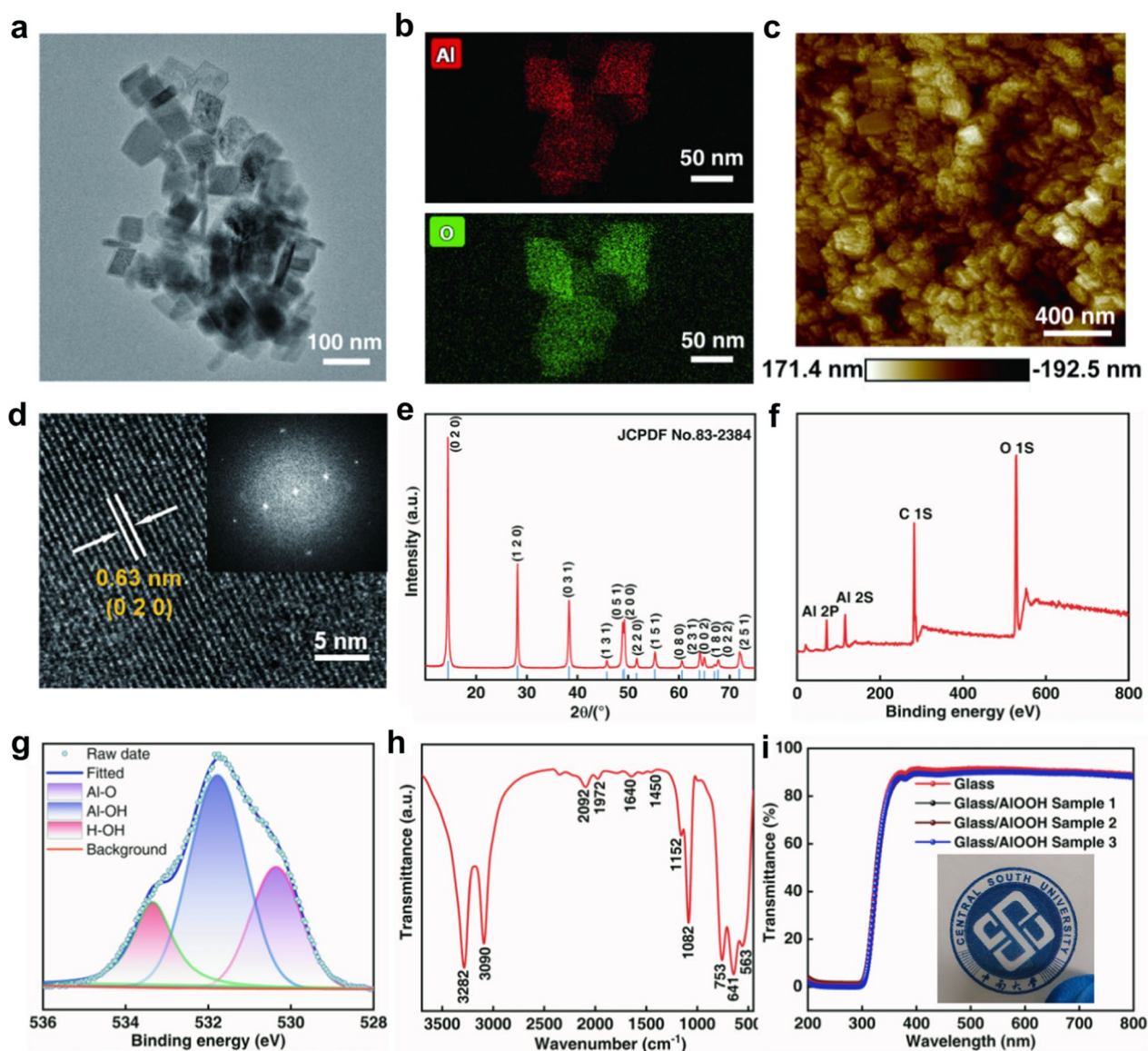


Fig. 2 Structure characterization of AlOOH. **a** Low-magnification TEM image of AlOOH nanosheets. **b** The corresponding element mapping of Al and O in AlOOH nanosheets. **c** AFM topography image of AlOOH film illustrating distribution and arrangement of AlOOH nanosheets in the film. **d** High-resolution TEM image showing the crystal lattice of AlOOH. The AlOOH crystal surface spacing is 0.63 nm, corresponding to the (0 2 0) crystal orientation. Inset: the corresponding FFT pattern. **e** XRD patterns of AlOOH film. **f** XPS analysis of AlOOH film. **g** O 1s core level spectra for the AlOOH film. **h** FTIR images of AlOOH film. **i** Transmittance spectra of Glass/AlOOH in the visible region; the CSU logo beneath the devices is clearly visible without any distortion owing to the excellent transparent properties of the device structure

device state switched from high resistance state to low resistance state. Subsequently, the low resistance state was maintained until the applied voltage exceeded the reset voltage ($V_{\text{reset}} \sim -1.2$ V), and the device gradually changed to the high resistance state. Finally, the device completely returned to the high resistance state at the applied voltage ~ -2.5 V. In general, the threshold voltage of the device is relatively small. Besides, it is worth noting that the device does not require a

positive-forming process with a large voltage sweep. This is correlated with the resistance change mechanism, because it is different from the conventional memristors which rely on oxygen vacancy conduction [44].

To reveal the physical process inside the device, the I-V curves is plotted in dual-logarithmic scales, where the fitting result of the I-V curve agrees with the space charge limited current (SCLC) model in this device (Fig. 3b),

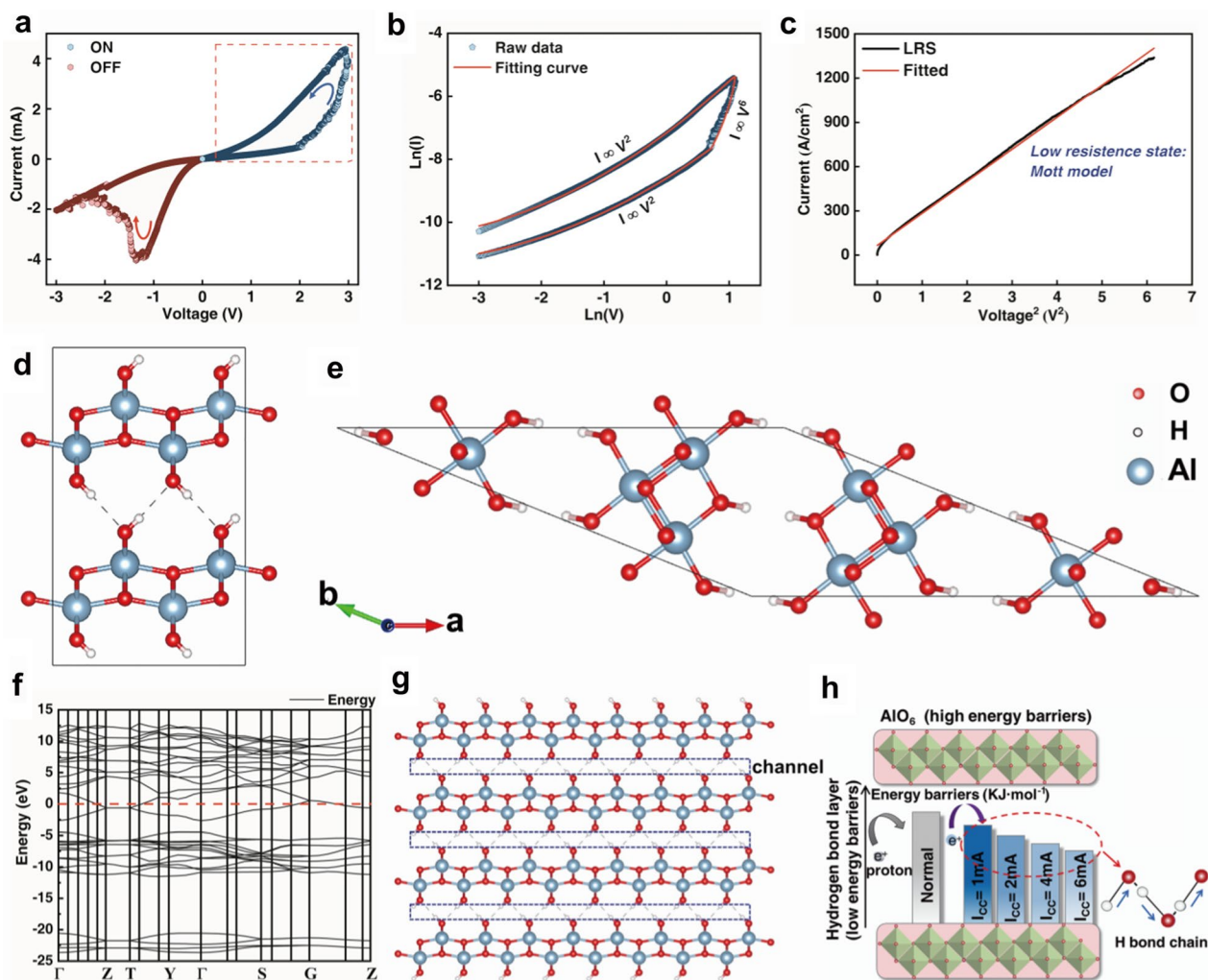


Fig. 3 Switching mechanism of Pt/AIOOH/ITO/PDMS device. **a** Typical current versus voltage (I - V) curves of the Pt/AIOOH/ITO/PDMS device in voltage sweeping mode at room temperature. A compliance current of 4 mA is used in set process. **b** The fitting slopes of the I - V curve for the red square area in **a**. **c** Fitting curve at the LRS portion showing Mott–Gurney behavior as the conduction mechanism. **d, e** The unoptimized (**d**) and fully optimized (**e**) models of AIOOH configuration respectively. **f** The band structure of AIOOH structure. **g** The formation of the pipe effect in the AIOOH material. **h** Schematic diagrams illustrating the proposed memristive switching mechanisms in AIOOH memristors. The reduction of O–H bond length with increasing I_{CC} could enhance the proton migration by reducing the potential barrier, thereby raising the conductivity

followed by the subsequent voltage scan curves of the device under different I_{CC} which share the same model. To reveal the intrinsic resistive switching behavior, the carrier mobility was calculated in the low resistance state. The transport behavior was fitted based on the Mott–Gurney law (Fig. 3c) [45].

$$I = \frac{9}{8} \varepsilon_r \varepsilon_0 \mu \frac{V^2}{d^3} \quad (1)$$

where μ is the carrier mobility, ε_r is the relative permittivity, ε_0 is the permittivity of free space, and d is the distance between electrodes. According to the fitting curve, the carrier mobility was determined to be $\approx 240 \text{ cm}^2 \text{ V}^{-1}$

s^{-1} , by using $\varepsilon_r = 8.5$ and $d = 0.3 \text{ } \mu\text{m}$. This value is comparable to the carrier mobility reported in semiconductor oxides from Additional file 1: Table S2 [46, 47].

Moreover, the mobility of between AIOOH layers is quantified through acoustic phonon scattering mechanism, where the structural optimizations and electronic structure calculations are performed based on density functional theory (DFT) as implemented in the Vienna Ab Initio Simulation Package (VASP) code based on the projector augmented wave (PAW) method with a cutoff energy of 600 eV^2 . The Brillouin zone sampling is carried out using the $(3 \times 3 \times 1)$ Monkhorst–Pack grids for surface and Gamma for the structure. The adopted crucial

parameters are concluded as follows: convergence tolerance of energy is 1×10^{-5} eV, maximum force $0.002 \text{ eV} \cdot \text{\AA}^{-1}$, and maximum displacement 0.002 \AA . The rest of the calculation details are described in the experimental part. The pristine and fully optimized models of ALOOH configuration are shown in Fig. 3d and e, respectively. The carrier mobility is calculated as follows (The detailed calculation can be referred to formula unit conversion in the Additional file):

$$\mu = \frac{e\hbar^3 \rho S_l^2}{k_B T m^* m_d E_l^2} \quad (2)$$

where S_l is the area of xy plane for the supercell, E_l is deformation potential constant, m_e is effective mass of electron, and m_d is average effective mass. The carrier mobility of ALOOH is determined to be $247 \text{ cm}^2 \text{ V}^{-1} \cdot \text{s}^{-1}$ according to the band structure of ALOOH structure in Fig. 3f, by using $e = 1.6 \times 10^{-19} \text{ C}$, $\hbar = 1.05 \times 10^{-34} \text{ J} \cdot \text{s}$, $K_B = 1.38 \times 10^{-23} \text{ J K}^{-1}$, $pS_l^2 = 4.6 \times 10^8 \text{ J m}^{-2}$, $m^* = 0.19 \text{ kg}$, $m_d = 0.516 \text{ kg}$, $E_l = 1.01 \times 10^{-19} \text{ J}$, which is consistent with the results of the carrier mobility calculated in the low resistance state, confirming the significance of hydrogen bond being responsible for the memristive behavior. The high carrier mobility is attributed to the formed pipe effect in the multilayer ALOOH material (Fig. 3g), which improves the transport properties of hydrogen proton. Moreover, the band structure where the K point defined in reciprocal lattice of the primitive cell is folded into point sitting at the Γ -Y-S branch of the supercell also confirms the pipe effect phenomenon. The result shows that the material with a very narrow band gap behaves the same as the band structure of conductor to some extent.

To further reveal and confirm the effect of hydrogen bonding on the memristive performance, ALOOH nanosheets was calcined at $600 \text{ }^\circ\text{C}$ for 2 h to avoid the effect of the hydrogen bond and consequently obtained Al_2O_3 nanosheets with the same shape. The XRD pattern result and morphology of Al_2O_3 nanosheets were presented in Additional file 1: Fig. S5a and b. Through the electrical measurements, it is found that the memristive performance of the Al_2O_3 device is completely different from that of the ALOOH device after eliminating the existence of hydrogen bonding, showing none multi-resistive state (Additional file 1: Fig. S5c), which further confirms the effect of hydrogen bonding on the memristive behavior through the experimental aspect.

Furthermore, the hydrogen ion in the hydrogen bond chain is highly itinerant with complex structural features, which can be feasible for proton conduction applications. Energy barriers of hydrogen transfer path on both perfect and vacancy-containing crystal structures were

computed through the theoretical aspect, whose energy barriers were generally below 21 kJ mol^{-1} in a perfect crystal, and 14 kJ mol^{-1} in a hydrogen vacancy-containing structure [48]. These low energy barriers are the desired indicators of high proton conductivity of ALOOH even at room temperature.

From the information gathered so far, we propose the working principles for the resistive switching in ALOOH memristor. Initially, under the action of an electric field, the hydrogen protons migrate, and part of the hydrogen vacancies are occupied by the injected hydrogen protons. As the applied voltage increases, the traps are gradually filled in the order of energy levels. Then, the barrier height gradually decreases, which leads to a decrease in impedance. As the impedance decreases, the channel current increases. Finally, the high and low resistance states are transformed. In the reverse sweep, the hydrogen protons trapped in the deep energy levels cannot be thoroughly released with decreasing applied voltage, which indicates that a portion of the traps are always filled and that the diminished barrier height cannot be recovered to the initial states, leading to the emergence of non-volatile behavior. The specific energy band diagram of the device is shown in Additional file 1: Fig. S6. The main mechanism causing proton transport is the Grotthuss mechanism [49], which is the proton transporting to a nearby site through hydrogen bonds. On the other hand, a secondary proton transport mode is ascribed to the protons and adsorb water molecules forming hydronium ions for transporting [50]. The existence of less adsorbed water has been proved by the XPS and FTIR characterization in Fig. 2.

The mechanism of multi-level switching by regulating I_{CC} is generally explained by the proposed formation of conductive filaments or conductive paths composed of oxygen vacancies or metal ions [14, 51]. As the increase of applied I_{CC} , thicker conductive filaments or more conductive paths are created inside devices, which further decrease the resistance value of the low-resistance state, consequently showing the multi-resistance state. According to the performance under multi-configured I_{CC} as well as the aforementioned resistance switching mechanism of the ALOOH device, it is obviously not feasible to explain the phenomenon of multi-level switching through the conventional filament mechanism. Therefore, another applicable and confirmed mechanism to explain the multi-level switching behavior for this device has been reasonably proposed. The conductivity difference of multilevel low resistance states is attributed to the change of the O-H bond length between ALOOH layers under different I_{CC} . When the device operated under high compliance current, the O-H bond length will decrease, resulting in the weaker bonding of hydrogen atoms and

enhancing the proton migration by lowering the energy barriers [52], thus increasing the conductivity (Fig. 3h). This is also applicable to explain the phenomenon that the device has a more stable multi-level switching than that of the traditional conductive filament memristor, showing the cyclic use of multi-resistance states.

Flexible resistance switching memory (RRAM) device with good biocompatibility is highly desirable due to their potential application in wearable and implantable electronics. These flexible AIOOH devices are insoluble compared with conventional biomemristors, so it is suitable for long-term detection and storage of human healthy. By evaluating the high performance of

the AIOOH nanosheets prepared through hydrothermal method, RRAM devices with multilevel Nonvolatile states is achieved. As a feasibility test, the ITO glass substrate was replaced by ITO-coated polydimethylsiloxane (PDMS) substrate with good flexibility to fabricate flexible memristor, while other remaining device fabrication processes and characterization studies were the same as described earlier, as illustrated in Fig. 4a.

In addition, to confirm the excellent biocompatibility of AIOOH nanosheets, the CCK-8 test is performed with detailed analysis as shown in Fig. 4b and Additional file 1: Table S3. The optical density (OD450) value measured at a wavelength of 450 nm showed the proliferation

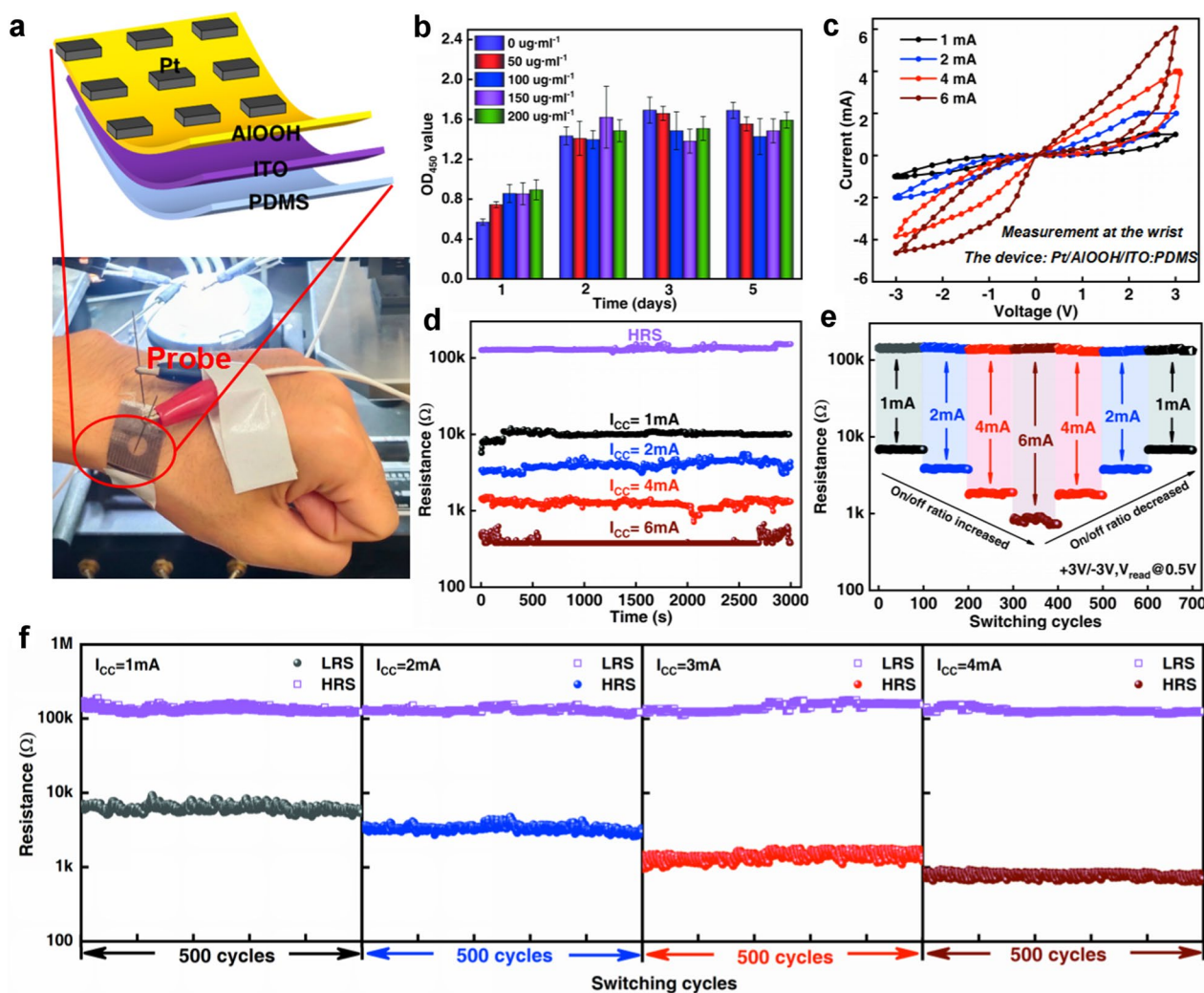


Fig. 4 Flexible Pt/AIOOH/ITO:PDMS memristive device characterization. **a** Schematic illustration of AIOOH flexible memristive device and the physical display of the flexible device. **b** The CCK-8 results for AIOOH nanosheets on different samples for 5 days. **c** Four different I-V curves of the device at different levels of I_{cc} (1 mA, 2 mA, 4 mA and 6 mA). **d** The retention time of the four resistance states all exceeding 3 × 10³ s. A read voltage of 0.5 V was used for the measurement. **e** Pt/AIOOH/ITO:PDMS memristive device stably circulate 700 cycles and the four storage states are completely reversible. **f** Repeatability test of the HRS and LRS values of the fabricated device under four different orders of I_{cc} (1 mA, 2 mA, 4 mA and 6 mA)

activity of the experimental group and the control group gradually increased with the increase of the incubation time, which confirms the non-toxic nature of AIOOH nanosheets for Raw264.7 cells. In addition, when the concentration of the AIOOH nanosheets solution was $200 \text{ ug}\cdot\text{mL}^{-1}$, the cell activity still did not change significantly and demonstrated no obvious dose effect, showing good biocompatibility. Therefore, the desired biocompatibility of AIOOH is showing the feasibility as a promising candidate material for wearable and implantable memristors.

Even in the case of flexible devices, four different memory states can be clearly distinguished with nonvolatile character, as shown in Fig. 4c. In addition, the flexible devices show the strong robustness and reliability of the four resistance states in this operating device. Figure 4d shows the retention time of the four resistance states with values exceeding $3 \times 10^3 \text{ s}$. And the device can stably circulate 700 cycles under the I_{CC} sweep of $1 \text{ mA} \rightarrow 2 \text{ mA} \rightarrow 4 \text{ mA} \rightarrow 6 \text{ mA} \rightarrow 4 \text{ mA} \rightarrow 2 \text{ mA} \rightarrow 1 \text{ mA}$ (Fig. 4e). Moreover, the endurance of the device under each individual I_{CC} of 1, 2, 4 and 6 mA has surpassed 500 cycles, with no degradation being observed (Fig. 4f). The four resistance states of the device can perfectly reflect the health of the human body. Taking the level of human hormone secretion as an example, the four states of the memristor can perfectly correspond to the five states of hormone secretion: trace amount (undetectable, $I_{CC} < 1 \text{ mA}$), low ($I_{CC} = 1 \text{ mA}$), normal ($I_{CC} = 2 \text{ mA}$), high ($I_{CC} = 4 \text{ mA}$), and excessive ($I_{CC} = 6 \text{ mA}$). The flexible biomemristor Pt/AIOOH/ITO/PDMS with other representative flexible biomemristors is compared in Additional file 1: Fig. S7 with respect to some crucial performance. Specifically, this flexible biomemristor Pt/AIOOH/ITO/PDMS has significant advantages in terms of cycle persistence and multi-bits of storage. Therefore, the device can simultaneously complete the information storage and the classification due to the multi-resistance states. In the future, the monitoring sensor composed of the memristors is expected to be realized, which can independently complete the integration of monitoring, storing, and classifying at the same time. It is expected to complete the human health monitoring and substantially reduce the incidence of major diseases.

The previous CCK-8 experiment results (Additional file 1: Table S3) showed that AIOOH showed excellent biocompatibility. In order to verify the feasibility of the application of the AIOOH flexible device in human body, the AIOOH flexible device was implanted in mice for biological experiments. The AIOOH flexible device was implanted subcutaneously in mice for long-term evaluation of its biological safety.

For the biocompatibility study, five male C57BL/6 mice aged 6 weeks were used. For subcutaneous implantation,

make a small incision at the back of the neck and insert the AIOOH flexible device into the wound. Then, suture the incision with absorbable suture, as shown in Fig. 5a. The skin tissue in contact with the AIOOH flexible device was collected from mice after incubation for 15, 30, 45 and 60 days to evaluate the biocompatibility of the AIOOH flexible device. The negative control is the skin tissue collected from mice that have never undergone any surgery or other experiments. All skin tissues were further stained with hematoxylin and eosin (H&E) for histological analysis, as shown in Fig. 5b–f. The experimental results showed that no obvious immune cell infiltration was observed in the surrounding tissues on the 15th, 30th, 45th and 60th days after implantation, indicating that the AIOOH flexible device has good compatibility with the host. In addition, the skin tissue near the AIOOH flexible device did not show dense fibrous capsule formation after 60 days, similar to the negative control skin tissue. This proves that AIOOH flexible memristor has potential for human application.

Finally, in order to evaluate whether the AIOOH flexible device is harmful to the main organs, samples of spleen, liver, lung, rein and heart were collected after 60 days of implantation and fixed with polyformaldehyde (in 4% PBS) for histological analysis. All the main organs of the heart, liver, spleen, lung and kidney of the mice after 60 days of implantation of the AIOOH flexible device were collected for H&E staining, as shown in Fig. 5g–i. No injury or inflammatory reaction was found in all these major organs. Although the test time in this part is only 2 months in mice, and there is no detailed characterization of the biological safety performance of the blood and other aspects of mice, it is the first of its kind to carry out the biological safety test in mice from the device level. The experimental results preliminarily confirmed that AIOOH flexible memristor has good biological safety and has the potential of implantable application in human body.

At present, research on biomemristors is mostly limited to the search for memristor materials. Biomaterials that can manufacture biomemristors mainly include natural biomaterials represented by proteins and inorganic materials with good biocompatibility. Natural biomaterials represented by proteins have become an important research direction in memristors due to low cost and degradability. However, there are many factors that affect the memristor characteristics of biomemristors represented by proteins during the preparation process, resulting in unstable memristors [7–9]. In addition, the working principles for the resistive switching in similar biomemristors are controversial and difficult to unify [14, 15]. The inorganic materials used in the preparation of biomemristors are mainly composed of oxides, and the switching

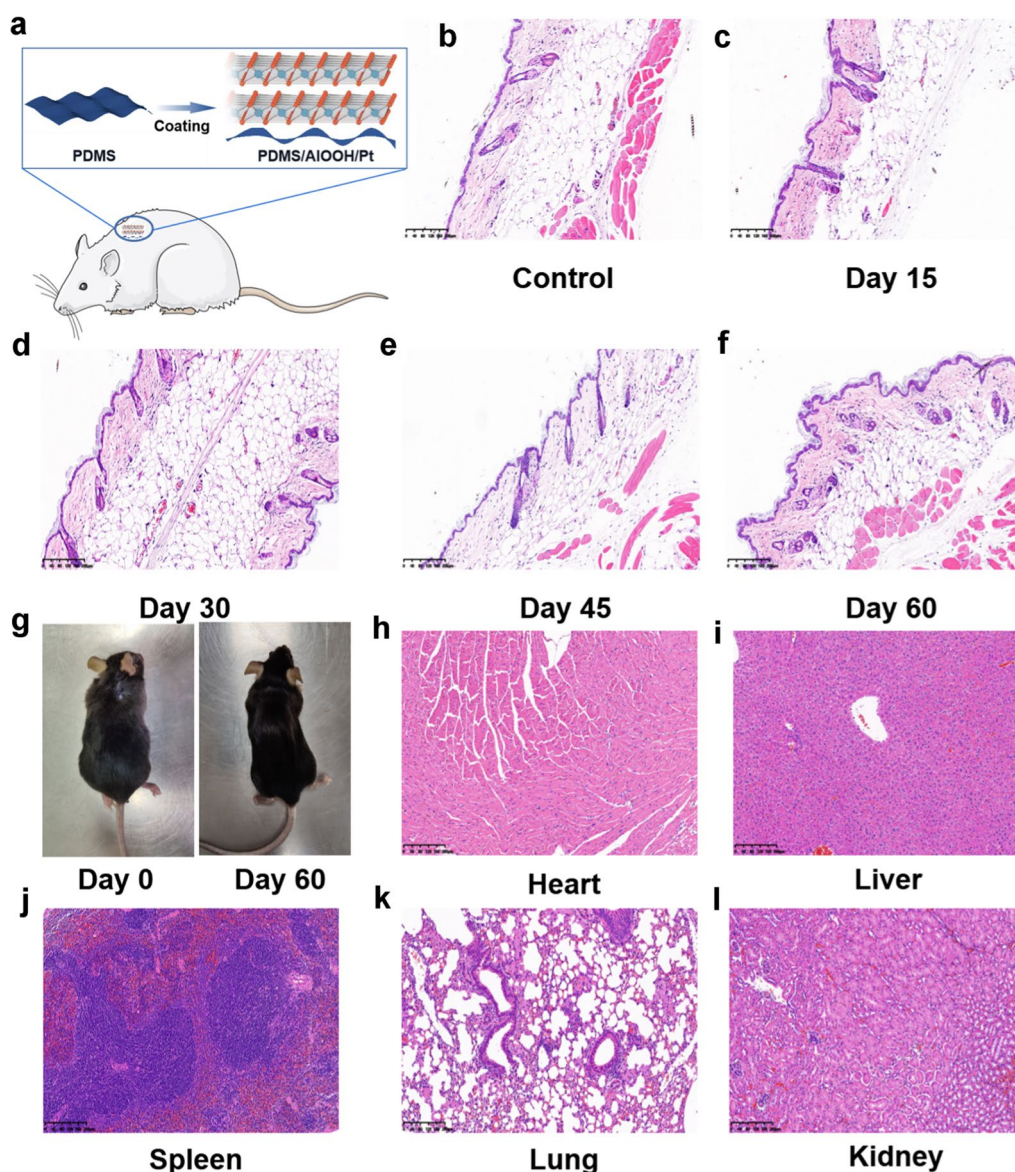


Fig. 5 Histological analysis of all major organs of mice after 60 days of implantation of AIOOH flexible device and skin tissue analysis of implanted sites at various stages after implantation of AIOOH flexible device: **a** schematic diagram of implanted AIOOH flexible device in mice; **b–f** mouse skin tissues in contact with AIOOH flexible devices collected after 15, 30, 45 and 60 days; **g** mice after implantation of AIOOH flexible devices at 0 and 60 days; **h, i** histological analysis of heart, liver, spleen, lung and kidney after 60 days of implantation of AIOOH flexible device

mechanism is mainly related to various defects such as oxygen vacancies [46]. The number and type of defects directly affect the characteristics of biomemristors, but it is difficult to stably control the distribution and quantity of defects during the production process. The switching mechanism of AIOOH biomemristor is relatively clear, and there are few defects that affect the memristor characteristics, making the memristor characteristics stable. Therefore, AIOOH is an excellent biomemristor material. However, in order to meet the biocompatibility

requirements of real-time and long-term monitoring of human health, it is necessary to further set up control experiments for comprehensive and detailed characterization, including the analysis of whether there is edema in cells from high magnification histology and the need for blood tests, statistics of whether various data such as hormones and biological enzymes are within the normal range, and finally carry out clinical experiments.

In conclusion, AIOOH nanosheets prepared by hydrothermal method initially show the stable resistance

switching performance for nonvolatile memory. For the configured Pt/AIOOH/ITO devices, performance of multi-level resistance switching memory has been achieved under different I_{CC} during the set process, with four states showing both high endurance ($>10^3$ cycles) and reliable retention ($>3.2 \times 10^3$ s). The memristive behavior of the device can be attributed to the hydrogen proton transport. Moreover, the flexible Pt/AIOOH/ITO:PDMS memristors is designed to achieve a high-performance memory device with excellent biocompatibility. These outstanding characteristics show that our flexible AIOOH memristive device is a promising candidate for applications in inexpensive flexible bio-compatible electronics. This work provides a new direction for the material selection of wearable and implantable memristors, where metal hydroxide represented by AIOOH is expected to be the potential candidate for building the next generation of wearable and implantable memristors.

Experimental section

Material synthesis [53, 54]

The 1 mol L^{-1} NaOH solution was slowly dropped into a 250 mL three-necked flask containing 0.025 mol L^{-1} AlCl_3 solution. The solution was adjusted to $\text{pH} = 10$, and the ultrasonic treatment was performed while mechanically stirring for 30 min. After the reaction was completed, the suspension was put into a reaction kettle lined with polytetrafluoroethylene, the reaction temperature was adjusted to 180°C , and the temperature was kept for 24 h. After the reaction was completed, it was washed and centrifuged three times with ethanol and deionized water, and then centrifuged at 60°C . After drying in 60°C , AIOOH nanosheets were finally obtained.

Device fabrications

AIOOH nanosheets were dispersed in the water. The concentration of AIOOH nanosheets dispersion liquid was 1 mg mL^{-1} . The AIOOH films were prepared by drop casting of the AIOOH dispersion liquid onto a ITO substrate. After drop casting, the sample was dried at room temperature, and this process was repeated for three times. Then, about 300 nm AIOOH film was obtained. The Pt electrode is grown by magnetron sputtering with the assistance of a shadow mask with a diameter of $10 \mu\text{m}$. In particular, the ITO:PDMS substrate is customized by Le Lin Technology Development Co., Ltd.

Cell culture

Raw 264.7 cells (5×10^3 cells per well, $100 \mu\text{L}$ per well) were cultured in Dulbecco's modified Eagle's medium (DMEM; Gibco) containing 10% fetal bovine serum (Gibco) and 1% penicillin/streptomycin (Gibco).

Raw264.7 cells were incubated at a humidity atmosphere containing 5% CO_2 at 37°C for 24, 48, and 72 h. For AIOOH nanosheets sterilized by 120°C , aqueous extractions with different concentrations (50, 100, 150 and $200 \mu\text{g mL}^{-1}$) were synthesized for raw 264.7 cells cell culture. Cell viability is equal to the absorbance ratio of the experimental group and the control group.

Cellular viability test (CCK-8) assay

At indicated time points, the samples were washed three times with PBS. Then $360 \mu\text{L}$ of medium with $40 \mu\text{L}$ of CCK-8 solution was added to each disk. After incubation for 2 h at 37°C , $100 \mu\text{L}$ of the incubated solution was transformed to a new 96-well plate, and the optical density (OD) value of the solution was measured with an ELISA plate reader (Varioskan Flash 3001, Thermo, Finland) at 450 nm wavelength.

Animal experiments

For biocompatibility studies, five 6-week-old male C57BL/6 mice were used. Dorsal hair was removed with the help of a 0.1 mm animal hair clipper. All animal studies were performed under protocols approved by the Shanghai Jiao Tong University Institutional Animal Care and Use Committee (Approval No. B-2021-009). The skin was cleaned with alcohol wetted cotton swab for 3 times. 4% Chloral Hydrate was used to induce anesthesia. For subcutaneous implantation, a small incision was made in the posterior neck and Pt/AIOOH/ITO was inserted into the wound. After that, the incision was closed with absorbable sutures. After implanting for 15, 30, 45 and 60 days, respectively, mice were sacrificed and the skin close to Pt/AIOOH/ITO were harvested and fixed with paraformaldehyde (4% in PBS) for histological analyses. To evaluate if the Pt/AIOOH/ITO is harmful to the major organs, spleen, liver, lung, rein, and heart samples after 60 days implanting were harvested and fixed with paraformaldehyde (4% in PBS) for histological analyses.

Electrical measurements

All electrical characterizations of the device were performed at ambient condition using a probe station and a Keithley 4200-SCS semiconductor parameter analyzer system equipped with our programming test software. The voltage signals designed for specific learning rules are applied to the ITO electrode, and the Pt electrode is grounded.

Material characterizations

The crystallization and phase structure of the fabricated AIOOH was carried out by X-ray diffraction (XRD) system (Empyren, PANalytical) and surface chemical states

were examined by X-ray photoelectron spectroscopy (XPS, 250Xi ESCALAB). Fourier transform infrared (FTIR) spectra were obtained using a Thermo Fisher Scientific ls-50 spectrometer in the range 400–4000 cm^{-1} at room temperature. The morphologies of the AIOOH were observed by scanning electron microscopy (SEM, TESCAN MIRA3 LMU). The high-resolution transmission electron microscope (HRTEM) was measured using a FEI Tecnai G2 F20. All the electrical measurements were performed on a probe station connected to a Keithley 4200-SCS semiconductor characterization system.

DFT method

The structural optimizations and electronic structure calculations are performed based on DFT as implemented in the Vienna Ab Initio Simulation Package (VASP) code [55], based on the projector augmented wave (PAW) method with a cutoff energy of 600 eV [56]. The configuration of AIOOH was fully optimized [55]. The generalized gradient form (GGA) of the exchange–correlation functional (Perdew–Burke–Ernzerhof 96, PBE) was adopted [57, 58]. A revised PBE generalized gradient approximation was used for the exchange–correlation [59, 60]. PBE sol functional has been introduced to improve the equilibrium properties of solids [61]. Valence-core interactions were described by projector-augmented-wave (PAW) pseudopotentials [62]. The Brillouin zone sampling is carried out using the $(3 \times 3 \times 1)$ Monkhorst–Pack grids for surface and Gamma for the structure [56]. The convergence tolerance of energy is 1×10^{-5} eV, maximum force is $0.002 \text{ eV} \cdot \text{\AA}^{-1}$, and maximum displacement is 0.002 \AA [56].

Supplementary Information

The online version contains supplementary material available at <https://doi.org/10.1186/s12951-023-02117-5>.

Additional file 1: Figure S1. The performance of various biomemristor devices were summarized. **Figure S2.** Presenting Different I-V Curves of under Different Compliance Currents (ICC). **Table S1.** Comparison of the memristive performance of implantable memristors. **Figure S3.** Morphology Characterization of AIOOH Film and AIOOH Nanosheets. **Figure S4.** Al_2O_3 Nanosheets Memristors. **Figure S6.** Corresponding conduction energy band profiles for the set (left) and reset (right). Formula Unit Conversion of formula/Eq. (2). **Table S2.** Carrier Mobility of Metal Oxides. **Table S3.** Raw data for the Cell Counting Kit-8 (CCK-8) tests. **Figure S7.** The Comparison Between AIOOH and Other Representative Biomemristors.

Acknowledgements

The project were financially supported by Natural Science Foundation of Changsha and Hunan Province, China (kq2202093, 2022JJ30722 and 2023JJ30690), the Opening Project of State Key Laboratory of High Performance Ceramics and Superfine Microstructures (SKL202202SIC), and the Start-Up Funds for Outstanding Talents in Central South University (202045007).

Author contributions

ZS, DN, HH and JY for the Conceptualization, Data curation, Formal analysis, and writing the original draft. XC, XZ, XH, and XT for the Investigation, Methodology. JY and HH for the Funding acquisition, Project administration, and Supervision. All authors read and approved the final manuscript. In addition, we wish to thank the timely help given by Shanghai Mifang Technology Co. Ltd. for joining the discussion of device design and test.

Data availability

All data in this study are available from the corresponding author upon reasonable request.

Declarations

Competing interests

The authors declared no competing financial interest.

Author details

¹Powder Metallurgy Research Institute, Central South University, Changsha 410083, China. ²School of Chemistry and Physics, QUT Centre for Materials Science, Queensland University of Technology, Brisbane, QLD 4001, Australia. ³Department of Orthopaedics, Shanghai Key Laboratory for Prevention and Treatment of Bone and Joint Diseases, Shanghai Institute of Traumatology and Orthopaedics, Ruijin Hospital, Shanghai Jiao Tong University School of Medicine, Shanghai 200025, China. ⁴Research Institute of Aerospace Technology, Central South University, Changsha 410083, China. ⁵State Key Laboratory of Powder Metallurgy, Hunan Key Laboratory of Advanced Fibers and Composites, State Key Laboratory of High Performance Ceramics and Superfine Microstructure, Research Institute of Aerospace Technology, Central South University, Changsha 410083, China.

Received: 20 June 2023 Accepted: 20 September 2023

Published online: 13 October 2023

References

- Linn E, Rosezin R, Kügeler C, Waser R. Complementary resistive switches for passive nanocrossbar memories. *Nat Mater*. 2010;9:403.
- Borghetti GS, Snider PJ, Kuekes JJ, Yang DR, Stewart RS, Williams, 'Memristive' switches enable 'stateful' logic operations via material implication. *Nature*. 2010;464:873.
- Yang JJ, Strukov DB, Stewart DR. Suppression of endurance degradation by utilizing oxygen plasma treatment in HfO₂ resistive switching memory. *Nat Nanotechnol*. 2013;8:13.
- Shi C, Hu F, Wu R, Xu Z, Shao G, Yu R, Liu XY. New silk road: from mesoscopic reconstruction/functionalization to flexible meso-electronics/ photonics based on cocoon silk materials. *Adv Mater*. 2021. <https://doi.org/10.1002/adma.202005910>.
- Sun B, Zhou G, Guo T, Zhou YN, Wu YA. Biomemristors as the next generation bioelectronics. *Nano Energy*. 2020;75: 104938.
- Yang SC, Zong MG, Yang LX. Research progress of protein-based memristor. *Acta Phys Sin*. 2020;69: 178702.
- Baek H, Lee C, Lim KI, Cho J. Resistive switching memory properties of layer-by-layer assembled enzyme multilayers. *Nanotechnol*. 2012;23: 155604.
- Jang SK, Kim S, Salman MS, Jang JR, Um YM, Tan L, Park JH, Choe WS, Lee S. Harnessing recombinant DnaJ protein as reversible metal chelator for a high-performance resistive switching device. *Chem Mater*. 2018;30:781.
- Lin Q, Hao S, Hu W, Wang M, Zang Z, Zhu L, Du J, Tang X. Human hair keratin for physically transient resistive switching memory devices. *J Mater Chem C*. 2019;7:3315.
- Moudgil A, Kalyani N, Sinsinbar G, Das S, Mishra P. S-layer protein for resistive switching and flexible nonvolatile memory device. *ACS Appl Mater Interfaces*. 2018;10:4866.
- Hosseini NR, Lee JS. Controlling the resistive switching behavior in starch-based flexible biomemristors. *ACS Appl Mater Interfaces*. 2016;8:7326.
- Sun B, Zhang X, Zhou G, Li P, Zhang Y, Wang H, Xia Y, Zhao Y. An organic nonvolatile resistive switching memory device fabricated with natural pectin from fruit peel. *Org Electron*. 2017;42:181.

13. Zhang C, Shang J, Xue W, Tan H, Pan L, Yang X, Guo S, Hao J, Liu G, Li R-W. Convertible resistive switching characteristics between memory switching and threshold switching in a single ferritin-based memristor. *Chem Commun.* 2016;52:4828.
14. Wang H, Meng F, Cai Y, Zheng L, Li Y, Liu Y, Jiang Y, Wang X, Chen X. Sericin for resistance switching device with multilevel nonvolatile memory. *Adv Mater.* 2013;25:5498.
15. Yan X, Li X, Zhou Z, Zhao J, Wang H, Wang J, Zhang L, Ren D, Zhang X, Chen J, Lu C, Zhou P, Liu Q. Flexible transparent organic artificial synapse based on the tungsten/egg albumen/indium tin oxide/polyethylene terephthalate memristor. *ACS Appl Mater Interfaces.* 2019;11:18654.
16. Park SP, Tak YJ, Kim HJ, Lee JH, Yoo H, Kim HJ. Analysis of the bipolar resistive switching behavior of a biocompatible glucose film for resistive random access memory. *Adv Mater.* 2018;30:1800722.
17. Hota MK, Bera MK, Kundu B, Kundu SC, Maiti CK. A natural silk fibroin protein-based transparent bio-memristor. *Adv Funct Mater.* 2012;22:4493.
18. Chen Z, Huang W, Zhao W, Hou C, Ma C, Liu C, Sun H, Yin Y, Li X. Ultra-fast multilevel switching in Au/YIG/n-Si RRAM. *Adv Electron Mater.* 2019;5:1800418.
19. Long B, Li Y, Jha R. Switching Characteristics of Ru/HfO₂/TiO₂-x/Ru RRAM devices for digital and analog nonvolatile memory applications. *IEEE Electron Device Lett.* 2012;33:706.
20. Liu SJ, Wang P, Zhao Q, Yang HY, Wong J, Sun HB, Dong XC, Lin WP, Huang W. Single polymer-based ternary electronic memory material and device. *Adv Mater.* 2012;24:2901.
21. Tunega D, Pašalić H, Gerzabek M, Lischka H. Theoretical study of structural, mechanical and spectroscopic properties of boehmite (γ -AlOOH). *J Phys: Condens Matter.* 2011;23:404201.
22. Zhang H, Li P, Cui W, Liu C, Wang S, Zheng S, Zhang Y. Synthesis of nanostructured γ -AlOOH and its accelerating behavior on the thermal decomposition of AP. *RSC Adv.* 2016;6:27235.
23. Yao Z, Pan L, Liu L, Zhang J, Lin Q, Ye Y, Zhang Z, Xiang S, Chen B. Simultaneous implementation of resistive switching and rectifying effects in a metal-organic framework with switched hydrogen bond pathway. *Sci Adv.* 2019;5:4515.
24. Li X, Shenashen MA, Mekawy M, Taniguchi A, Ei-Safty SA. Aluminum hydroxide nanosheets with structure-dependent storage and transportation toward cancer chemotherapy. *Int J Inorg Mater.* 2020;35:250.
25. Sun B, Ji Z, Liao Y-P, Wang M, Wang X, Dong J, Chang CH, Li R, Zhang H, Nel AE. Engineering an effective immune adjuvant by designed control of shape and crystallinity of aluminum oxyhydroxide nanoparticles. *ACS Nano.* 2013;7:10834.
26. Selim MS, Hamouda H, Hao Z, Shabana S, Chen X. Design of γ -AlOOH, γ -MnOOH, and α -Mn₂O₃ nanorods as advanced antibacterial active agents. *Dalton Trans.* 2020;49:8601.
27. Li X, Zhang L, Guo R, Chen J, Yan X. A flexible transient biomemristor based on hybrid structure HfO₂/BSA: Au double layers. *Adv Mater Technol.* 2020;5:2000191.
28. Lv Z, Wang Y, Chen Z, Sun L, Wang J, Chen M, Xu Z, Liao Q, Zhou L, Chen X. Phototunable biomemory based on light-mediated charge trap. *Adv Sci.* 2018;5:1800714.
29. Shi C, Wang J, Sushko ML, Qiu W, Yan X, Liu XY. Silk flexible electronics: from bombyx mori Silk Ag nanoclusters hybrid materials to mesoscopic memristors and synaptic emulators. *Adv Funct Mater.* 2019;29:1904777.
30. Dang B, Wu Q, Song F, Sun J, Yang M, Ma X, Wang H, Hao Y. A bio-inspired physically transient/biodegradable synapse for security neuromorphic computing based on memristors. *Nanoscale.* 2018;10:20089.
31. Wang H, Zhu B, Wang H, Ma X, Hao Y, Chen X. Ultra-lightweight resistive switching memory devices based on silk fibroin. *Small.* 2016;12:3360.
32. Xing Y, Shi C, Zhao J, Qiu W, Lin N, Wang J, Yan XB, Yu WD, Liu XY. Mesoscopic-functionalization of silk fibroin with gold nanoclusters mediated by keratin and bioinspired silk synapse. *Small.* 2017;13:1702390.
33. Zhu JX, Zhou WL, Wang ZQ, Xu HY, Lin Y, Liu WZ, Ma JG, Liu YC. Flexible, transferable and conformal egg albumen based resistive switching memory devices. *RSC Adv.* 2017;7:32114.
34. Yong J, Hassan B, Liang Y, Ganesan K, Rajasekharan R, Evans R, Egan G, Kavehei O, Li J, Chana G, Nasr B, Skafidas E. Hydrogen enhances strength and ductility of an equiatomic high-entropy alloy. *Sci Rep.* 2017;7:1.
35. Wu Z, Zhuo Q, Sun T, Wang Z. Mechanical properties of epoxy resins reinforced with synthetic boehmite (AlOOH) nanosheets. *J Appl Polym Sci.* 2015;132:41409.
36. Marchesini FA, Irusta S, Querini C, Miró E. Spectroscopic and catalytic characterization of Pd-In and Pt-In supported on Al₂O₃ and SiO₂, active catalysts for nitrate hydrogenation. *Appl Catal A.* 2008;348:60.
37. Dhonge BP, Mathews T, Sundari ST, Krishnan R, Balamurugan A, Kamruddin M, Subbarao R, Dash S, Tyagi A. Synthesis of Al₂O₃ thin films using laser assisted spray pyrolysis (LASP). *Appl Surf Sci.* 2013;265:257.
38. Zhang Q, Wang T, Fu W, Duan X, Xuan S. Facet-dependent performance of hydroxylated anodic boehmite for catalyzing gaseous formaldehyde oxidation. *Catal Lett.* 1904;2018:148.
39. Gao C, Yu X-Y, Xu R-X, Liu J-H, Huang X-J. AlOOH-reduced graphene oxide nanocomposites: one-pot hydrothermal synthesis and their enhanced electrochemical activity for heavy metal ions. *ACS Appl Mater Interfaces.* 2012;4:4672.
40. Xu Z, Yu J, Low J, Jaroniec M. Microemulsion-assisted synthesis of mesoporous aluminum oxyhydroxide nanoflakes for efficient removal of gaseous formaldehyde. *ACS Appl Mater Interfaces.* 2014;6:2111.
41. Abdollahifar M, Hidayan M, Jafari P. The role anions on the synthesis of AlOOH nanoparticles using simple solvothermal method. *BOL SOC ESP CERAM V.* 2018;57:66.
42. Rajasekaran S, Simanjuntak FM, Panda D, Chandrasekaran S, Aluguri R, Saleem A, Tseng TY. Fast, highly flexible, and transparent TaOx-based environmentally robust memristors for wearable and aerospace applications. *ACS Appl Electron Mater.* 2020;2:3131.
43. Simanjuntak FM, Ohno T, Samukawa S. Influence of rf sputter power on ZnO film characteristics for transparent memristor devices. *APL Adv.* 2019;9:105216.
44. Yin X, Wang Y, Chang TH, Zhang P, Li J, Xue P, Long Y, Shohet JL, Voyles PM, Ma Z. Memristive behavior enabled by amorphous-crystalline 2D oxide heterostructure. *Adv Mater.* 2020;32:2000801.
45. Li C, Hu M, Li Y, Jiang H, Ge N, Montgomery E, Zhang J, Song W, Dávila N, Graves CE. Analogue signal and image processing with large memristor crossbars. *Nat Electron.* 2018;1:52.
46. Yeh CC, Zan HW, Soppera O. Solution-based micro-and nanoscale metal oxide structures formed by direct patterning for electro-optical applications. *Adv Mater.* 2018;30:1800923.
47. Dasgupta NP, Sun J, Liu C, Brittan S, Andrews SC, Lim J, Gao H, Yan R, Yang P. 25th anniversary article: semiconductor nanowires—synthesis, characterization, and applications. *Adv Mater.* 2014;26:2137.
48. Jiang Y, Xie Y, Guo H. A computational study of energy barriers of structural transformations and hydrogen transfer in boehmite. *RSC Adv.* 2018;8:2377.
49. Agmon N. The grothuss mechanism. *Chem Phys Lett.* 1995;244:456.
50. Kreuer KD, Rabenau A, Weppner W. Vehicle mechanism, a new model for the interpretation of the conductivity of fast proton conductors. *Angew Chem Int Edit.* 1982;21:208.
51. Prakash A, Park J, Song J, Woo J, Cha E-J, Hwang H. Demonstration of low power 3-bit multilevel cell characteristics in a TaOx-based RRAM by stack engineering. *IEEE Electron Device Lett.* 2014;36:32.
52. Wang R, Yoshino T. Electrical conductivity of diaspore, δ -AlOOH and ϵ -FeOOH. *Am Mineral.* 2021;106:774.
53. Chen XY, Huh HS, Lee SW. Hydrothermal synthesis of boehmite (γ -AlOOH) nanoplatelets and nanowires: pH-controlled morphologies. *Nanotechnology.* 2007;18:285608.
54. Hou H, Xie Y, Yang Q, Guo Q, Tan C. Hydrothermal synthesis of boehmite (γ -AlOOH) nanoplatelets and nanowires: pH-controlled morphologies. *Nanotechnol.* 2005;16:741.
55. Kresse G, Hafner J. Ab initio molecular dynamics for liquid metals. *Phys Rev B.* 1993;47:558.
56. Iniguez J, Vanderbilt D, Bellaiche L. First-principles study of (BiScO₃)_{1-x}-(PbTiO₃)_x piezoelectric alloys. *Phys Rev B.* 2003;67:224107.
57. Hammer B, Hansen LB, Nørskov JK. Improved adsorption energetics within density-functional theory using revised Perdew-Burke-Ernzerhof functionals. *Phys Rev B.* 1999;59:7413.
58. Asahi R, Mannstadt W, Freeman AJ. Optical properties and electronic structures of semiconductors with screened-exchange LDA. *Phys Rev B.* 1999;59:7486.
59. Perdew JP, Burke K, Ernzerhof M. Generalized gradient approximation made simple. *Phys Rev Lett.* 1996;77:3865.
60. Perdew JP, Ruzsinszky A, Csonka GI, Vydrov OA, Scuseria GE, Constantin LA, Zhou X, Burke K. Restoring the density-gradient expansion for exchange in solids and surfaces. *Phys Rev Lett.* 2008;100:136406.
61. Blöchl PE. Projector augmented-wave method. *Phys Rev B.* 1994;50:17953.

62. Csonka GI, Perdew JP, Ruzsinszky A, Philippsen PH, Lebègue S, Paier J, Vydrov OA, Ángyán JG. Assessing the performance of recent density functionals for bulk solids. *Phys Rev B*. 2009;79: 155107.

Publisher's Note

Springer Nature remains neutral with regard to jurisdictional claims in published maps and institutional affiliations.

Ready to submit your research? Choose BMC and benefit from:

- fast, convenient online submission
- thorough peer review by experienced researchers in your field
- rapid publication on acceptance
- support for research data, including large and complex data types
- gold Open Access which fosters wider collaboration and increased citations
- maximum visibility for your research: over 100M website views per year

At BMC, research is always in progress.

Learn more biomedcentral.com/submissions

